

DANCING IN THE DARK: NEW BROWN DWARF BINARIES FROM KERNEL PHASE INTERFEROMETRY¹

BENJAMIN POPE

Sydney Institute for Astronomy, School of Physics, University of Sydney, NSW 2226, Australia

FRANTZ MARTINACHE

National Astronomical Observatory of Japan, Subaru Telescope, Hilo, HI 96720, USA

PETER TUTHILL

Sydney Institute for Astronomy, School of Physics, University of Sydney, NSW 2226, Australia

Draft version February 28, 2013

ABSTRACT

This paper revisits a sample of ultracool dwarfs in the Solar neighborhood previously observed with the Hubble Space Telescope’s NICMOS NIC1 instrument. We have applied a novel high angular resolution data analysis technique based on the extraction and fitting of kernel phases to archival data. This was found to deliver a dramatic improvement over earlier analysis methods, permitting a search for companions down to projected separations of ~ 1 AU on NIC1 snapshot images. We reveal five new close binary candidates and present revised astrometry on previously-known binaries, all of which were recovered with the technique. The new candidate binaries have sufficiently close separation to determine dynamical masses in a short-term observing campaign. We also present four marginal detections of objects which may be very close binaries or high contrast companions. Including only confident detections within 19 parsecs, we report a binary fraction of at least $\epsilon_b = 17.2^{+5.7}_{-3.7}\%$. The results reported here provide new insights into the population of nearby ultracool binaries, while also offering an incisive case study of the benefits conferred by the kernel phase approach in the recovery of companions within a few resolution elements of the PSF core.

Subject headings: techniques: interferometric — techniques: image processing — techniques: high angular resolution — stars: low-mass — stars: formation — (stars:) brown dwarfs

1. INTRODUCTION

A detailed picture of multiplicity is an essential element to understanding low-mass stars and brown dwarfs. Binary systems present an opportunity to determine model-independent dynamical masses when both astrometry and radial velocity data are available. Systems so characterized may then become part of the foundations for the construction of an observationally constrained mass-luminosity-age sequence applicable across the entire class.

Furthermore, the statistical properties of populations of low mass binaries have profound implications on the basic physics of star formation and solar system assembly. Multiplicity rates are a key discriminant between hypotheses about the formation and evolution of low mass systems, as discussed in Burgasser et al. (2007). Two main mechanisms have been proposed for the formation of brown dwarfs in the field: embryo ejection, and gravoturbulent collapse (Basu 2012). Specifically, the embryo ejection hypothesis predicts a low binarity incidence ($\sim 8\%$) (Bate 2012), which conflicts with the observed bi-

nararity rate ($\sim 15\%$) (Reid & Hawley 2005). Mapping the incidence of binarity, and in particular extending completeness to smaller orbital separation is therefore of interest in establishing the primary formation mechanism of field brown dwarfs.

Snapshot imaging is a straightforward way to discover new multiple systems. Intrinsically faint and red, L-dwarfs present challenging targets for ground based observations, typically requiring laser guide star (LGS) adaptive optics (AO). Space telescopes naturally offer high Strehl ratio imaging at diffraction-limited resolution, with the major departures from ideal performance arising from field-dependent PSF changes, spacecraft jitter, and slow optical drift from thermally induced breathing modes of the mechanical structures.

Imaging campaigns with the HST have demonstrated notable success in prospecting for companions to cool objects, providing high quality diffraction-limited images of a large number of targets (Reid et al. 2006a, 2008). These campaigns have shed light on the population of cool dwarfs in the Solar neighborhood.

The simplest and most widely used method for detection of companions in snapshot imaging essentially relies on direct visual examination of images. Obvious companions are quickly identified, and traditional astronomical image analysis tools, namely aperture photometry and centroiding, provide the important astrometric and photometric characteristics of the target. Faint or close-in companions are, however, easily missed in a visual search

bjsp@physics.usyd.edu.au
 frantz@naoj.org
 p.tuthill@physics.usyd.edu.au

¹ Based on observations performed with the NASA/ESA Hubble Space Telescope. The Hubble observations are associated with proposal ID 10143 and 10879 and were obtained at the Space Telescope Science Institute, which is operated by the Association of Universities for Research in Astronomy, Inc., under NASA contract NAS 5-26555.

and identifying such objects requires more sophisticated computational techniques.

For example, some stellar images exhibit an elongation along one axis as noted by Reid et al. (2006a) which may be suggestive of the presence of a barely-resolved companion. Subtraction of a model PSF has been exploited to infer the presence of a companion (Krist et al. 1998; Pravdo et al. 2004; Dieterich et al. 2012), although the performance of this approach is arguably poor, and furthermore it weakly constrains the relative photometry and astrometry. We propose to look at the same images from an interferometric standpoint, leveraging the exquisite level of calibration this technique offers.

For the detection and characterization of companions at small angular separations, non-redundant masking (NRM) interferometry used in conjunction with AO has demonstrated outstanding performance, e.g. in Tuthill et al. (2006); Lloyd et al. (2006); Kraus & Ireland (2012). The key underpinning such successes has been the robust, self-calibrating nature of the observables recovered from NRM interferometry, and in particular the *closure phase*, first suggested for the radio (Jennison 1958) and later exploited in the optical (Baldwin et al. 1986). Imaging systems where the phase on any given baseline in the pupil is disturbed by random phase errors from atmospheric or instrumental aberrations suffer from degraded performance. However by summing phases around closed loops of non-redundant baselines, these random phasors cancel out and the resulting closure phases are extremely robust to wavefront aberrations. NRM interferometry from the ground (Tuthill et al. 2000) relies heavily on closure phase for high-contrast detection, and there are plans to extend the technique to space platforms (Sivaramakrishnan et al. 2009). Recent observations achieved with this technique reported by Lloyd et al. (2006); Martinache et al. (2007); Ireland et al. (2008); Kraus et al. (2008) and Martinache et al. (2009) demonstrate that the level of calibration achieved with interferometric measurements permits the detection of companions at scales at or even somewhat beyond the diffraction limit of the imaging system. Recently, NRM interferometry succeeded in providing evidence for a low-luminosity companion in the transitional disk host systems T Cha (Huélamo et al. 2011) and LkCa 15 (Kraus & Ireland 2012).

It has recently been demonstrated that if a conventional (full-aperture) PSF is of sufficient quality (wavefront residual errors typically $\lesssim \lambda/4$), an analogous set of high-quality interferometric observables can be extracted from the images (Martinache 2010). These new quantities are the *kernel phases*, and represent a generalization of the idea of closure phase to a redundant pupil configuration. The major advance offered by kernel phase interferometry is that it is not restricted to non-redundant pupils. In brief, for small wavefront errors (i.e. high Strehl ratio), the phase errors in the pupil plane can be related to those in the Fourier plane by a linear operator. The kernel or null-space of this operator therefore singles out a subspace of baseline phases which are not affected by this error, which can then play the same role as closure phases in providing a robust set of observables to constrain image structure. Kernel phases were first successfully extracted from HST/NICMOS data on a single target by Martinache (2010), demonstrating sig-

nificant improvement over more traditional data analysis (Pravdo et al. 2004). The technique has now also been successfully applied to ground based AO observations (Martinache 2011).

This paper revisits a sample of nearby ultracool dwarfs observed by the Hubble Space Telescope NICMOS NIC1 camera and first presented in Reid et al. (2006a) and Reid et al. (2008). Our analysis allows dramatic extensions to the discovery space for putative companions, and in particular explores separation ranges down to 1 AU on targets located within 20 parsec. Section 2 provides an overview of the dataset and introduces the methods used for our new analysis. Section 3 discusses the results of the kernel phase analysis for the entire sample and implications for the astrophysical interpretation of brown dwarf formation.

2. SAMPLE AND METHODS

2.1. Sample of Ultracool Dwarfs

This study focuses on two samples of ultracool dwarfs, observed with the HST/NICMOS NIC1 camera, and whose properties were reported by Reid et al. (2006a) and Reid et al. (2008). Each target was observed in two filters: F110W and F170M, which correspond loosely to the astronomical *J* and *H* bands. These differ in that the *J* and *H* bands sample atmospheric transmission windows, which do not constrain space-based observations. We will use *J* and *H* as shorthands for F110W and F170M respectively, but the difference should be noted. Table 1 summarizes the observational properties of the combined sample as stated in Table 1 of Reid et al. (2006a) and Table 1 of Reid et al. (2008).

In addition to detecting several binaries by traditional data analysis methods, these authors also provide a list of 43 and 26 apparently unresolved objects in the 2006 and 2008 samples respectively, which we revisit in this paper. All ten of the previously resolved binaries were independently recovered with kernel phases, and for all we report significantly improved astrometric precision. In addition to confirming the technique and software on an unambiguous sample, the dramatic improvements to the binary parameters offer the chance to determine orbital elements and therefore dynamical masses. Both the detections and the remaining unresolved binaries are used in quantitative exploration of the performance limitations of kernel phase analysis in the recovery of high contrast systems.

2.2. Kernel Phase Analysis

Kernel phase analysis follows the principles introduced in Martinache (2010). The first step is to generate a model of the pupil of the imaging system as seen from the detector. This task is straightforward based on information contained in the TinyTim v. 7.2 PSF simulation package for NIC1 (Krist et al. 2011), available at tinytim.stsci.edu. For kernel phase analysis, the model pupil is discretized into a square grid array of 72 sub-apertures with a unit spacing $1/12$ th that of the pupil diameter (cf. Figure 1). Regions of the primary blocked by spiders or the secondary mirror are not sampled, and one can also observe that the unit baseline imposed by this sampling of the pupil imposes an outer working angle of $6\lambda/D$.

This geometry fills the (u, v) -plane with a regular grid of 176 distinct sample points at a cadence of 12 points across the diameter. The transfer matrix that relates instrumental phase errors to spurious (u, v) -phase information is therefore a 72×176 rectangular matrix, whose SVD reveals 36 non-zero singular values (that is exactly one half of the entire number of sample points in the pupil), leaving $176 - 36 = 140$ independent kernel phase relations. Kernel phase analysis can therefore recover $140/176 = 80\%$ of the available phase information present in the quantized grid.

The specific discretization chosen was found to have relatively little impact on the performance of the algorithm. If instead we adopt a finer-sampled pupil model with 20 points across the diameter, we get 1516 kernel phases out of 1632 distinct baselines, leading to a 93% phase recovery. We analyzed a portion of our dataset with this finer 20 point sampling and found little improvement in the quality of fit or precision in parameter estimation, though we note somewhat better agreement between H and J bands with the finer pupil model using Levenberg-Marquardt model fitting. Because the finer grid analysis was computationally expensive but yielded only a small change in fitted binary parameters, it was judged that application over a large grid to fit the available data was unwarranted. We have therefore chosen the coarser model for our fitting routines, but note that more computer time may produce some improvements with a finer pupil model. For application to wider separation binaries, however, the finer model would be strictly required: if we have p points across the pupil, Nyquist’s sampling theorem imposes an outer working angle $p\lambda/2D$. If this condition is not met, the Fourier plane fringes will not be well-sampled and parameter estimates will be subject to aliasing or may not be recovered at all.

A shorter wavelength of observation delivers an increase of angular resolution, but with the same level of optical aberration, this also precipitates a greater degree of image degradation (lower Strehl ratio). When considering residual phase noise, we therefore expect that the kernel phase signal-to-noise will be accordingly higher for images taken at longer wavelengths.

We are furthermore limited by the fact that we only have single snapshots of each target: without multiple frames it is difficult to calibrate systematic errors and explore statistical uncertainties on the kernel phase observables. We therefore selected a sample of stars for which we could see no PSF abnormality or obvious Fourier phase structure, and repeatedly applied a Levenberg-Marquardt fitting algorithm to the raw kernel phase data to attempt to find binary companions. Those targets for which no companion model was significantly preferred over a single source were deemed to be “unresolved”. We then used this unresolved population to establish uncertainties as ensemble standard deviations for each kernel phase, which in turn enables quantification of significance in subsequent explorations entailing χ^2 fitting. The results presented here could be considerably improved with the design of an observational campaign at the outset which delivers better diversity, by exploiting multiple exposures and dedicated point source calibrators. A more comprehensive understanding of systematic errors and noise estimates for individual targets would yield more

sensitive limits on detection and better errors on fitted parameters.

2.3. Bayesian Methods

A binary system at any one epoch can be characterized by its angular separation δ , position angle θ and contrast ratio c . The likelihood of a binary model with these parameters given the set of kernel phases $\{K\phi_j\}$ is related to the χ^2 statistic by

$$L(\delta, \theta, c | \{K\phi_j\}) \propto \exp(-\chi^2/2). \quad (1)$$

When normalized, this likelihood is the joint density probability function for all three parameters. When calculating χ^2 , we found it necessary to add an additional systematic error term in quadrature to bring the minimum reduced χ^2 down to 1. Confidence intervals for any individual parameter can be calculated by integrating over the two other parameters. After this *marginalization*, we estimate the parameter and its uncertainty from the mean and the standard deviation of the 1-D marginal distribution respectively.

The approach closely follows established practice with closure-phase in NRM-interferometry for the characterization of binaries (Martinache et al. 2009). When applied to our sample HST imaging data set, the final results from our algorithm were: (1), confirmation of binaries already identified with other methods; (2), the determination of statistically sound constraints on the binary parameters; and (3), a robust statistical estimate for the probability that signals extracted from any given system betray the presence of a companion or can be attributed to noise.

The sampling and integration of the likelihood function given in Equation 1 is in general difficult, and is typically performed by a computationally-expensive grid integration or a Monte Carlo Markov Chain (MCMC) random sampling method. In this paper we apply a recently developed alternative, namely nested sampling. This method, proposed by Skilling (2004), uses an unusual change of variables to calculate the model evidence. It has recently seen a surge of interest; e.g. for cosmological model fitting (Mukherjee et al. 2006; Mukherjee & Parkinson 2008), and the analysis of simulated gravitational wave data (Aylott et al. 2009; Feroz et al. 2009).

The key idea of nested sampling is to populate the allowed prior space with a large number (~ 100) of ‘active points’ which are initially chosen at random and subsequently evolved towards ensemble states of successively higher likelihood using MCMC methods. Our implementation was based on Sivia & Skilling (2006) and ultimately yielded a statistical representation of the likelihood space which could be used for binary hypothesis testing and estimation of model parameter values and their uncertainties. Although a number of alternate gradient-descent and MCMC methods were benchmarked, nested sampling was found to be computationally the most efficient. A global binarity analysis of the entire sample in both the J and H bands could be accomplished quickly, however for objects which are in the barely resolved limit, there are well known strong parameter degeneracies – particularly between separation and brightness of a companion. This ambiguity conflates

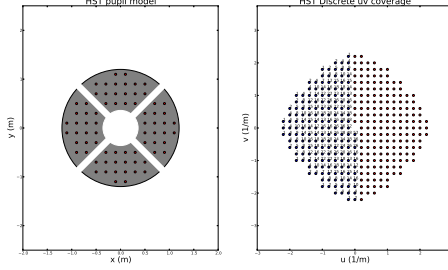


Figure 1. Diagrams showing (left) the discretized pupil model used for kernel phase analysis and (right) the resultant (u, v) sampling points.

bright close companion models with somewhat more distant fainter companion models, considerably diminishing the astrophysical utility of the findings.

In addition to separately fitting image data in J and H bands, nested sampling was fast enough to enable joint four-parameter fitting of both images simultaneously $\mathcal{M}(\delta, \theta, c_H, c_J)$. The ambiguity in separation/contrast from separate fitting was found to be greatly ameliorated by the covariance of separation with contrast. Joint fitting enforces identical separation between bands, greatly restricting the size of the χ^2 valley of degeneracy with contrast ratio. These findings are promising for the coming generation of Integral Field Unit cameras working with extreme AO systems which naturally deliver spatio-spectral data cube observations.

For the joint fitting, an additional error term was added in quadrature to represent unknown noise sources. This was found iteratively such that each band separately had a minimum reduced χ^2 of 1 at the best joint fit parameters. In cases where the existing error estimates resulted in a minimum reduced $\chi^2 < 1$, no adjustment was made.

For this study, we searched a delimited parameter space for companions. We initially searched up to a contrast ratio of 200, somewhat beyond the limits established in Section 3.4. Candidate binaries were then compared to Plots 2 and 3 to establish significance. The range of separation explored ran from 30 to 200 mas and all position angles were considered.

3. RESULTS AND DISCUSSION

Images for all objects in Table 1 in the two filter bands (F110W and F170M) were recovered in digital form from the HST MAST Archive, where they are listed under Proposals 10143 and 10879. All data were processed using our kernel phase techniques, and in the discussion which follows, we divide our results into three subsections: 3.1, binaries already reported; 3.2, new binaries uncovered by kernel phase; 3.3 marginal detections meriting further study; and 3.4, sample detection thresholds and the incidence of unresolved sources.

3.1. Known binaries

In all cases where companions were reported by Reid et al. (2006a) or Reid et al. (2008), our new analysis independently recovered strong systematic signals confirming binarity. We therefore confirm all previously reported detections, and we stress that our analysis was blind in the sense that no prior knowledge was employed in our search.

Table 1
Sample of unresolved L-dwarfs from Reid et al. (2006a) and Reid et al. (2008) (after line break)

| 2 MASS name | Sp. type | J | H | K |
|--------------------------|----------|--------|--------|-------|
| 2MASS J00361617+18211104 | L3.5 | 12.47 | 11.59 | 11.06 |
| 2MASS J00452143+1634446 | L0 | 13.06 | 12.06 | 11.37 |
| 2MASS J01075242+0041563 | L8 | 15.82 | 14.51 | 13.71 |
| 2MASS J01235905-4240073 | M8 | 13.15 | 12.47 | 12.04 |
| 2MASS J01550354+0950003 | L5 | 14.82 | 13.76 | 13.14 |
| 2MASS J02132880+4444453 | L1.5 | 13.51 | 12.77 | 12.24 |
| 2MASS J03140344+1603056 | L0 | 12.53 | 11.82 | 11.24 |
| 2MASS J03552337+1133437 | L6 | 14.05 | 12.53 | 11.53 |
| 2MASS J04390101-2353083 | L6.5 | 14.41 | 13.37 | 12.81 |
| 2MASS J04455387-3048204 | L2 | 13.41 | 12.57 | 11.98 |
| 2MASS J05002100+0330501 | L4 | 13.67 | 12.68 | 12.06 |
| 2MASS J05233822-1403022 | L2.5 | 13.12 | 12.22 | 11.63 |
| 2MASS J06244595-4521548 | L5 | 14.48 | 13.34 | 12.60 |
| 2MASS J06523073+4710348 | L4.5 | 13.55 | 12.37 | 11.69 |
| 2MASS J08251968+2115521 | L7.5 | 15.12 | 13.79 | 13.05 |
| 2MASS J08354256-0819237 | L5 | 13.15 | 11.95 | 11.16 |
| 2MASS J08472872-1532372 | L2 | 13.52 | 12.63 | 12.05 |
| 2MASS J09083803+5032088 | L7 | 14.56 | 13.47 | 12.92 |
| 2MASS J09111297+7401081 | L0 | 12.92 | 12.20 | 11.75 |
| 2MASS J09211410-2104446 | L2 | 12.78 | 12.15 | 11.69 |
| 2MASS J10452400-0149576 | L1 | 13.13 | 12.37 | 11.81 |
| 2MASS J10484281+0111580 | L1 | 12.92 | 12.14 | 11.62 |
| 2MASS J10511900+5613086 | L2 | 13.24 | 12.42 | 11.90 |
| 2MASS J11040127+1959217 | L4 | 14.46 | 13.48 | 12.98 |
| 2MASS J11083081+6830169 | L0.5 | 13.14 | 12.23 | 11.60 |
| 2MASS J12130336-0432437 | L5 | 14.67 | 13.68 | 13.00 |
| 2MASS J12212770+0257198 | L0 | 13.17 | 12.41 | 11.95 |
| 2MASS J14283132+5923354 | L5 | 14.78 | 13.88 | 13.27 |
| 2MASS J14482563+1031590 | L5 | 14.56 | 13.43 | 12.68 |
| 2MASS J15074769-1627386 | L5 | 12.82 | 11.90 | 11.30 |
| 2MASS J15394189-05200428 | L3.5 | 13.92 | 13.06 | 12.58 |
| 2MASS J15525906+2948485 | L1 | 13.48 | 12.61 | 12.03 |
| 2MASS J16580380+7027015 | L1 | 13.31 | 12.54 | 11.92 |
| 2MASS J17054834-0516462 | L0.5 | 13.31 | 12.54 | 12.03 |
| 2MASS J17312974+2721233 | L0 | 12.09 | 11.39 | 10.91 |
| 2MASS J17534518-6559559 | L4 | 14.10 | 13.11 | 12.42 |
| 2MASS J18071593+5015316 | L1.5 | 12.96 | 12.15 | 11.61 |
| 2MASS J19360262-5502367 | L4 | 14.49 | 13.63 | 13.05 |
| 2MASS J20575409-0252302 | L1.5 | 13.12 | 12.27 | 11.75 |
| 2MASS J21041491-1037369 | L2.5 | 13.84 | 12.96 | 12.36 |
| 2MASS J22244381-0158521 | L4.5 | 14.05 | 12.80 | 12.01 |
| 2MASS J23254530+4251488 | L7.0 | 15.51 | 14.46 | 13.81 |
| 2MASS J23515044-2537367 | L0.5 | 12.46 | 11.73 | 11.29 |
| 2MASS J002424.6-015819 | M9.5 | 11.86 | 11.12 | 10.58 |
| 2MASS J010921.7+294925 | M9.5 | 12.91 | 12.16 | 11.68 |
| 2MASS J022842.4+163933 | L0 | 13.17 | 12.33 | 11.82 |
| 2MASS J025114.8-035245 | L3 | 13.08 | 12.26 | 11.65 |
| 2MASS J025503.5-470050 | L8 | 13.23 | 12.19 | 11.53 |
| 2MASS J031854.0-342129 | L7 | 15.53 | 14.31 | 13.48 |
| 2MASS J044337.6+000205 | M9 | 12.52 | 11.80 | 11.17 |
| 2MASS J083008.3+482848 | L8 | 15.44 | 14.34 | 13.68 |
| 2MASS J085925.4-194926 | L7 | 15.51 | 14.44 | 13.73 |
| 2MASS J102248.2+582545 | L1 | 13.50 | 12.64 | 12.16 |
| 2MASS J102552.3+321235 | L7 | 15.91: | 15.59: | 15.07 |
| 2MASS J104307.5+222523 | L8 | 15.95 | 14.75 | 13.99 |
| 2MASS J105847.8-154817 | L3 | 14.18 | 13.24 | 12.51 |
| 2MASS J115539.5-372735 | L2 | 12.81 | 12.04 | 11.46 |
| 2MASS J120358.1+001550 | L4 | 14.01 | 13.06 | 12.48 |
| 2MASS J130042.5+191235 | L1 | 12.71 | 12.07 | 11.61 |
| 2MASS J142131.5+182741 | L0 | 13.23 | 12.43 | 11.94 |
| 2MASS J142528.0-365023 | L3 | 13.75 | 12.58 | 14.49 |
| 2MASS J143928.4+192915 | L1 | 12.76 | 12.04 | 11.55 |
| 2MASS J150654.4+132106 | L3 | 13.41 | 12.41 | 11.75 |
| 2MASS J151500.9+484739 | L6 | 14.06 | 13.07 | 12.57 |
| 2MASS J172103.9+334415 | L3 | 13.58 | 12.92 | 12.47 |
| 2MASS J200250.7-052152 | L6 | 15.32 | 14.23 | 13.36 |
| 2MASS J202820.4+005227 | L3 | 14.30 | 12.38 | 12.79 |
| 2MASS J214816.3+400359 | L6.5 | 14.15 | 12.78 | 11.77 |
| 2MASS J223732.5+392239 | M9.5 | 13.35 | 12.68 | 12.15 |

In common with closure phases, non-zero excursions in the kernel phases encode information about asymmetric structures, although the abstracted nature of the observable makes for significant challenges in intuitive data presentation. One approach to present the way a binary signal is encoded upon the kernel phases, and the fingerprint match of this complex function to the actual recorded data, is to simply plot the best-fit model quantities against the observed data in a correlation diagram.

Figures 6 and 5 present such a diagram of the binary model fit against extracted kernel phase data for two illustrative cases: previously-known binaries 2M 0700+3157 and 2M 0147-4954. The one-to-one correspondence line is overplotted, delineating the locus of perfect fit.

Kernel phase analysis has yielded greatly improved astrometric precision on most previously known binary systems. Whereas previous studies, relying on visual analysis and PSF subtraction, quoted separations to the nearest 10 mas and position angle to $\sim 1^\circ$, kernel phase delivers about one order of magnitude better precision. All fitted binary parameters agree, typically to within 1σ , when separate fits to J and H band kernel phases are computed. Table 2 gives final best fit parameters from the simultaneous J/H four-parameter fit. In many cases, the best fits differ from previously published estimates, sometimes very substantially (although formal errors were not quoted in Reid et al. (2006a) or Reid et al. (2008)).

Counterintuitively, for some of the most readily apparent binaries (e.g. 2M 0004-4044, 0025+4759, 0915-0422 and 2152+0937), kernel phase methods proved problematic and could fail to converge to a good fit. This was particularly true for well-separated, low contrast systems which are most easily discerned by simple inspection. Wide binaries induce phase curvature not well sampled by our pupil model, and for these cases, a direct fit to the squared visibilities was performed. Visibility data were calibrated by dividing by the ensemble means over the sample, with dimensionless errors of ~ 0.05 added in quadrature. As with the kernel phases, statistical analysis was based on nested sampling and the results also yielded overwhelming improvements in astrometric precision.

The PSF of the individual target 2M 0004-4044 was truncated at the edge of the image, presumably due to spacecraft mis-pointing, and therefore did not permit a useful kernel phase fit in H band. Nevertheless, a J band kernel fit was found to agree well with the parameters published in Reid et al. (2006a), and likewise a joint visibility fit agreed well in both bands. The results of the visibility fit are quoted in Table 2. It is unclear, however, what effect the data edge truncation may have on our interferometric observables and therefore the values given in Table 2 are likely to be subject to an additional unknown error for this system.

Example correlation diagrams and a corresponding NICMOS image are shown in Figure 4 and Figure 5. Note that while the PSFs of the primary and companion overlap and are difficult to visually distinguish, they permit a clear kernel phase fit with very precise parameter estimates.

3.2. Discovery of New Binary Candidates

Table 3 reports five firm binary candidates not detected in the original Reid et al. (2006a) or Reid et al. (2008) studies, but recovered at very high 99.9% confidence from our kernel phase analysis (with the exception of 2M 0045+1634 for which the detection confidence was only 99%). Correlation plots for all of these are displayed as Figures 8 to 11.

Reid et al. (2006a) noted three targets which exhibited broad PSFs, however they went on to report these stars had “... no evidence for the presence of a secondary component, and the broader profiles are probably an instrumental effect.” These were 2M 1507-1627 and 2M 1936-5502, with a PSF FWHM of 2.47 pixels (106 mas) and 2M 0036+1821 with a FWHM of 2.56 pixels (110 mas), as opposed to the FWHM of 2.3-2.4 pixels found through the rest of the unresolved sample. Our kernel phase analysis identifies two of these as binary candidates: 2M 1936-5502, and 2M 0036+1821. We note that for both of these, the kernel phase signal-to-noise ratio is only of order 2, and they exhibit a correspondingly noisy correlation plot.

2M 1936-5502 supported an alias fit at around 225° position angle, and the contrast in H band was very poorly constrained. This may well be considered the most marginal fit reported in this section. Nevertheless, both bands support overlapping position angle modes at 330° , and this object was considered for further study.

For 2M 0036+1821, there are two distinct χ^2 minima in H band, one of which overlaps precisely with the single distinct minimum from the J band data. In assigning parameter estimates for this object, we have assumed some uncalibrated source of noise affected the H band and have therefore restricted the parameter space deliberately to contain only that region around the high-significance J band χ^2 detection.

The third target with a reported broad PSF, 2M 1507-1627, shows marginally-significant companion fits with parameters which are inconsistent between J and H bands. Until additional data can be recovered with higher signal-to-noise, we classify this object to be unresolved with no companion.

A companion to 2M 0036+1821 was also reported by Bernat et al. (2010) with non-redundant masking interferometry in K band with the laser guide star adaptive optics system on the Hale Telescope at Palomar Observatory. From data taken in September 2008 (some 3.5 years after the HST observations), these authors report a contrast ratio of 13.1 ± 3.1 and separation of 90 ± 11 mas at a position angle of $114^\circ \pm 5$. Although changes in the binary separation parameters are to be expected with progress in an orbit, the markedly different contrast ratio when compared to our fit in Table 3 is, at first glance, hard to reconcile. However we note that both studies employ similar fundamental methodologies and are affected by the strong separation-contrast ratio degeneracy previously discussed. In particular, the work of Bernat et al. (2010) observed only in the K_s band and therefore enjoyed none of the advantages offered by dual wavelengths in lifting the ambiguity discussed in Section 2.3. Indeed, in their discussion an alternate detection at 25:1 contrast and 243 mas with equal probability is debated and ruled out based on the HST archival data. To test the hy-

Table 2
Model Parameters for Known L-Dwarf Binaries

| 2 MASS Number | Sep. (mas) | Pos. angle (degrees) | Contrast Ratio (J) | Contrast Ratio (H) |
|------------------------|---------------|-------------------------|-----------------------|-----------------------|
| 0004-4044 ^a | 84.6±0.2 | 224.6±0.1 | 1.04±0.01 | 1.02±0.02 |
| 0025+4759 ^a | 329.0±0.3 | 233.04±0.06 | 1.32±0.04 | 1.03±0.04 |
| 0147-4954 | 139.8±0.1 | 72.66±0.05 | 2.37±0.09 | 2.06±0.06 |
| 0429-3123 | 525.2±1.2 | 285.3±0.2 | 3.51±0.1 | 2.82±0.06 |
| 0700+3157 | 179.6±0.5 | 105.8±0.1 | 4.52±0.07 | 3.81±0.03 |
| 0915-0422 ^a | 738.6±0.15 | 26.89±0.01 | 1.114±0.002 | 1.264±0.002 |
| 1707-0558 | 1009.5±1.0 | 34.9±0.05 | 10.6±0.15 | 7.5±0.2 |
| 2152+0937 ^a | 253.7±0.09 | 94.5±0.02 | 1.09±0.03 | 1.15±0.03 |
| 2252-1730 ^b | 125.9±0.4 | 353.5±0.1 | 2.46±0.01 | 3.395±0.03 |
| 2255-5713 | 178.6±0.4 | 172.7±0.1 | 5.05±0.08 | 4.33±0.02 |

^a Low contrast: fit with visibilities. See Section 3.1.

^b This object is the subject of Reid et al. (2006b).

pothesis that both the Bernat et al. (2010) companion and the one reported here are consistent with the same degree of phase asymmetry, we re-fit our kernel phase data with an enforced higher contrast ratio above 10:1. This immediately resulted in much larger best-fit separations, approaching those from Bernat et al. (2010), and we therefore conclude that the two studies have probably identified the same companion.

All of these systems were originally assigned spectral classes in Reid et al. (2006a), which must be altered to reflect the discovery of new companions. A similar approach is taken here, using tabulated $J - H$ colours (Pecaut & Mamajek in preparation) to determine new spectral classes, taking into account the contrast ratio found at each wavelength. The class assigned to the secondary from its colour is compared to the expected contrast with the primary as a function of spectral class, and found in each case to be relatively consistent. These classes, being based on contrasts which are themselves subject to error, are accurate only to within one division. Of special interest are 2M 2351-2537 and 2M 1936-5502. In the former case, Reid et al. (2008) reassigned the spectral type from L0.5 determined in Reid et al. (2006a) to M8, and excluded the system from their 20-parsec catalogue of L dwarfs on these grounds. On the other hand, Andrei et al. (2011) classify it as L0.0 based on precision photometry. Revealing it as a binary system, its colours and luminosity imply that both primary and secondary must be early-L dwarfs, with possible classes L0 and L1.

Given the uncertainty in contrast in the 2M 1936-5502 system, no accurate spectral type can be determined for the secondary component. If the high-contrast fit is confirmed, then the secondary must have a spectral type later than T9. A brown dwarf of Y class is possible in principle, but coeval companionship to an early-L primary seems unlikely if the primary is a brown dwarf. If this is the case, then the companion may be of planetary mass. On the other hand, if the primary is a star, then this could be an evolved companion of brown dwarf mass as discussed in Kirkpatrick et al. (2012). We note that Faherty et al. (2012) present a new parallax distance for this object of 15.08 ± 1.2 pc, which compares well with the spectroscopic distance estimate in Reid et al. (2006a) and comparatively poorly with new estimates we calculate with the revised tables of Pecaut & Mamajek (in preparation), from which we obtain a distance of

18.6 ± 2.8 pc, though we note that the measurement is still consistent with the quoted uncertainties.

For 2M 0036+1821, the distance is known from trigonometric parallax to be 8.77 ± 0.06 pc (Dahn et al. 2002). The angular separation of 44.5 mas therefore equates to 0.4 AU projected physical separation. This is therefore one of the closest projected separations of any resolved brown dwarf binary. The 90 mas separation from Bernat et al. (2010) gives typical binary orbital periods of $\sim 2-3$ years, while on the other hand our 44.5 mas separation gives orbits of $\lesssim 1$ year. Ignoring the changes in separation (due to degeneracy errors), the position angle change of 84° observed between the HST and Palomar datasets could be consistent with more than one orbit in the former case or several orbits in the latter: either is consistent with the data and a more rapid observing cadence is required to unambiguously follow the orbit in this particular system.

Excepting 2M 0036+1821 and 2M 1936-5502, the distances of other objects are known from spectroscopic parallax and are therefore subject to change depending on whether the system is found to be a binary. In general, discovery of a companion implies a higher total luminosity for the system, and therefore a greater distance. Table 3 lists recalculated spectroscopic distances, with standard 15% uncertainties. In particular, the reassignment of 2M 2351-2537 as an L0/L1 binary moves it back into the 20-parsec L dwarf sample, while 2M 0045+1634 and 2M 2028+0052 fall beyond 20 parsecs. The spectroscopic distance of 9.2 ± 1.4 pc for 2M 0036+1821 agrees well with the spectroscopic parallax of 8.77 pc.

Our kernel phase re-analysis of the HST archive does not detect a binary reported by Bernat et al. (2010) in 2M 0355+1133 at 90 mas separation. One explanation may be that at the HST epoch the projected separation was smaller and therefore unresolved. This is nevertheless included in the discussion of binarity fraction in Section 4.3. The object 2M 0045+1634 was observed by Stumpf et al. (2010) with differential spectral imaging using the HST NICMOS camera; a PSF variation was noted but no other signal found in the vicinity of the brown dwarf.

Thus four of the five detections reported in Table 3 can be considered new, and we confirm the previously-reported detection in 2M 0036+1821 albeit with discrepant best-fit contrast. All detections are significantly

below the formal diffraction limit and at separations of the order of the detector plate scale, which is 43.1 mas/pixel. It is therefore unsurprising that the candidate binaries are a subject to parameter correlation and substantial uncertainties. These may therefore require confirmation and accurate constraint of parameters found with follow-up observations employing a larger telescope.

3.3. Possible New Companions at Higher Contrasts

Estimates in Martinache (2011) suggested the possibility of detections at contrast ratios greater than 50:1 using kernel phases. The recent discovery of planetary-mass companions to brown dwarfs (Todorov et al. 2010) indicates that these objects exist and are at least common enough that in a sufficiently large dataset candidates may be found. On the other hand, given the parameter degeneracy, it is possible that some high contrast detections revealed by these techniques are in fact very close low contrast binaries. Owing to this large uncertainty, no attempt has been made to assign separate magnitudes or spectral classes to the faint companions identified in this section.

A study of all the unresolved objects in our sample extending to a contrast of 100 revealed four objects with fits agreeing in position angle between bands: 2M 0314+1603, 2M 1539-0520, 2M 0830+4828 and 2M 0109+2949.

These objects were then subjected to a nested sampling joint fit to examine correlation at best fit. In the extreme contrast-separation regime probed here, the parameters show very pronounced degeneracy and it is impossible to reliably distinguish between high contrast objects further out and lower contrast objects closer in, even using both J and H bands. No error was added in quadrature, as in each case the kernel phases were already over-fit with reduced $\chi^2 < 1$.

2M 0314+1603 is the best of the candidates in Table 5 and exhibits excellent correlation in J band. Nevertheless, while H band data favours a χ^2 minimum at this same position angle, it is unconstrained in contrast ratio and reliably runs off to high contrast in each attempted fit. Likewise 2M 1539-0520 supported good correlation diagrams but a surprisingly large discrepancy in contrast ratio between bands. This is likely to be the result of a strongly degenerate fit which constrains neither contrast well; the contrast ratios should therefore not be considered well-determined.

With a J contrast > 160 , as a coeval companion to a brown dwarf this can only be a planetary mass object. On the other hand, it is possible that the L primary may be a star at the low-mass limit of the main sequence and its companion is itself an evolved brown dwarf. Such a system is still of considerable interest: as noted in Dieterich et al. (2012), low-mass binary systems tend to be of equal mass, increasingly so at lower primary masses. Accordingly, few brown dwarf secondaries to main sequence primaries are known, especially at close separations. This is the low-mass end of the ‘brown dwarf desert’ first identified by Marcy & Butler (2000), which has since become the subject of intense study (Grether & Lineweaver 2006; Allen et al. 2007; Kraus et al. 2008; Deleuil et al. 2008; Kraus et al. 2011; Dieterich et al. 2012; Evans et al. 2012). A confirmation of the status of this system, regardless of result, would

therefore be a potentially significant finding.

Correlation plots for the marginal detections are shown in Figures 12 to 15.

3.4. Survey Confidence and Detection Limits

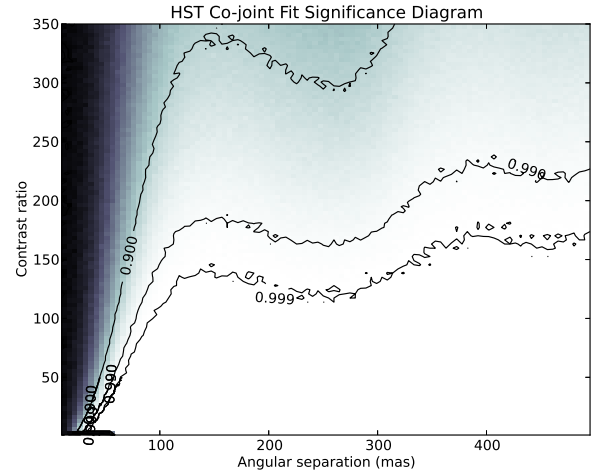


Figure 2. HST snapshot contrast-detection limits for co-joint fitting as a function of separation, averaged over position angle. The 90%, 99% and 99.9% contours are overplotted with labels. Paler regions indicate higher significance.

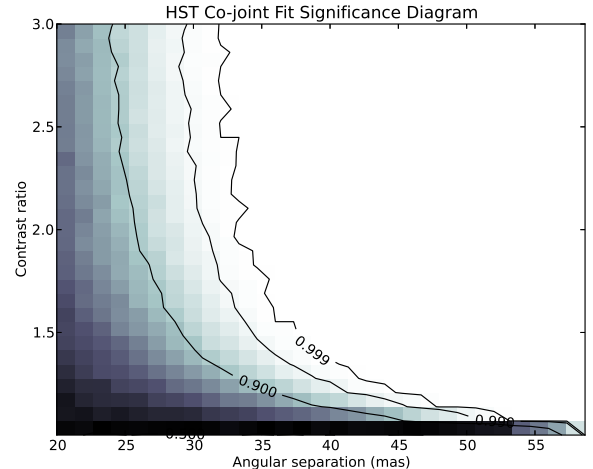


Figure 3. HST snapshot contrast-detection limits for co-joint fitting as a function of separation, averaged over position angle. The 90%, 99% and 99.9% contours are overplotted labels. Paler regions indicate higher significance. This figure represents a simulation of the region near the origin of Figure 2 with a finer sample grid. Note the turnaround at low contrast: kernel phase performs poorly at detecting very-low-contrast companions.

In order to quantify our survey detection threshold as a function of model parameters, we performed a Monte-Carlo study simulating detection of a population of model binaries. We ran 100 simulations, adding a binary at each point on a grid in separation, position angle and contrast ratio, in both J and H bands, as a co-joint fit. We then added Gaussian noise randomly to each of these, with the distribution given by our measured

Table 3
Model Parameters for New L-Dwarf Binary Candidates

| 2 MASS Number | Spectral Type | Distance (pc) | Sep. (mas) | Pos. angle (degrees) | Contrast Ratio (<i>J</i>) | Contrast Ratio (<i>H</i>) | <i>J</i> mag | <i>H</i> mag |
|-------------------------|------------------|--------------------------|---------------|-------------------------|--------------------------------|--------------------------------|-----------------|-----------------|
| 0036+1821 ^{ab} | L3.5 | 8.77 ± 0.06 ^d | 44.5±1.2 | 198.4±1.3 | 1.85±0.3 | 2.9±1.1 | 12.47 | 11.59 |
| A | L4 | | | | | | 12.93 | 11.91 |
| B | L5-6 | | | | | | 13.6 | 13.06 |
| 0045+1634 ^c | L0 | 26.8 ± 4.0 | 50.3±0.7 | 300.6±2.5 | 1.11±0.02 | 1.12±0.03 | 13.06 | 12.06 |
| A | L0 | | | | | | 13.75 | 12.75 |
| B | L0 | | | | | | 13.87 | 12.87 |
| 1936-5502 ^a | L4 | 15.08 ± 1.2 ^e | 67.1±6.4 | 330.9±1.0 | 17.7±3.9 | 35.5±8.1 | 14.49 | 13.63 |
| A | L4 | | | | | | 14.54 | 13.66 |
| B | (T-Y) | | | | | | 17.67 | 17.53 |
| 2028+0052 | L3 | 26.1 ± 3.9 | 45.8±1.2 | 107.7±1.1 | 1.52±0.1 | 3.1± 0.5 | 14.3 | 12.38 |
| A | L3 | | | | | | 14.85 | 12.7 |
| B | L4 | | | | | 15.3 | 13.9 | |
| 2351-2537 | L0.5 | 17.8 ± 2.7 | 63.3±0.3 | 348.8±0.3 | 2.4±0.1 | 2.24±0.2 | 12.46 | 11.73 |
| A | L0 | | | | | | 12.84 | 12.13 |
| B | L1 | | | | | | 13.79 | 13.006 |

^a Reid et al. (2006a) listed these objects as having a significant PSF abnormality. A third object showing such an abnormality, 2M 1507-1627, does not show a kernel phase binary fit.

^b Bernat et al. (2010) detected this binary with Palomar adaptive optics aperture masking.

^c This object was observed with spectral differential imaging by Stumpf et al. (2010). A PSF broadening was noticed but no other unambiguous signal was detected.

^d This distance is known from trigonometric parallax to be 8.77 ± 0.06 pc (Dahn et al. 2002).

^e Using the newer spectral class - absolute magnitude tables from Pecaut & Mamajek (in preparation), we revise the Reid spectroscopic distance from 15.4 pc to 18.6 ± 2.8 pc.

Table 4
Mass Estimates for New L-Dwarf Binary Candidates

| 2 MASS Number | $M_{0.5Gyr}$ M_{\odot} | M_{1Gyr} M_{\odot} | M_{5Gyr} M_{\odot} |
|------------------|-----------------------------|---------------------------|---------------------------|
| 0036+1821 A | 0.049 | 0.064 | 0.073 |
| B | 0.045 | 0.060 | 0.071 |
| 0045+1634 A | 0.07 | 0.078 | 0.081 |
| B | 0.07 | 0.078 | 0.081 |
| 1936-5502 A | 0.049 | 0.064 | 0.073 |
| B | | | |
| 2028+0052 A | 0.052 | 0.066 | 0.074 |
| B | 0.049 | 0.064 | 0.073 |
| 2351-2537 A | 0.07 | 0.078 | 0.081 |
| B | 0.059 | 0.072 | 0.075 |

Table 5
Model Parameters for Marginal High Contrast Companions

| 2 MASS Number | Separation (mas) | Position angle (degrees) | Contrast Ratio (<i>J</i>) | Contrast Ratio (<i>H</i>) |
|------------------|---------------------|-----------------------------|--------------------------------|--------------------------------|
| 0109+2949 | 49 ± 13 | 268 ± 3 | 40 ± 25 | 43 ± 29 |
| 0314+1603 | 124 ± 16 | 227 ± 2 | 70 ± 10 | > 160 |
| 0830+4828 | 48 ± 9 | 120 ± 3 | 29 ± 16 | 14 ± 11 |
| 1539-0520 | 35 ± 5 | 332 ± 5 | (4 ± 3) | (28 ± 16) |

error distribution as discussed in Section 2.2. The detection rates as a function of separation and contrast are averaged over position angle (distributions were found to be azimuthally symmetric). Quantitative detection thresholds were formulated from comparison of the binary model χ^2 to the null hypothesis. This method is similar to that used in Martinache (2010). We also examined the low-contrast, low separation domain in which we have found many of our binaries with a finer sample

grid. The contrast detection limit curves turn around at very low contrasts, as kernel phase performs poorly in discerning very-low-contrast companions, which give rise to highly-symmetrical images with a weak Fourier phase signal. This is true of any phase-based method, as the Fourier phases encode information about spatial asymmetries in a source image, and this problem therefore affects closure phases in NRM interferometry as well. This therefore places a lower limit on the contrasts detectable at very small separations. The contrast thresholds obtained from these studies are shown in Figures 2 and 3 respectively. Our estimates here compare favourably with the kernel phase contrast detection limits predicted for the Keck Telescopes in Martinache (2011), which are at best closer to 50:1. This very high sensitivity with the HST is unsurprising, given the high quality of the wavefront, and this technique therefore holds great promise in its application to similar snapshot samples.

Over any companion detection hangs the question as to whether the pair of stars imaged are physically associated, or whether they merely happen to lie along the same line of sight but are otherwise unrelated. It is therefore important to establish the expected count of background stars in the direction of each star, which will in general differ according to the star's position, owing to shape of the Galaxy and the distribution of dust.

The *Galaxia* software package (Sharma et al. 2011) is a synthetic survey tool, which calculates the expected density of Galactic stars at a given magnitude in a given band along a given line of sight. This was applied in 0.1-square-degree regions around the coordinates of each binary candidate, searching for background stars between 12th and 18th apparent magnitude in *J* and *H* bands. For a canonical 12th magnitude primary, these span the contrast range from 1 to 100, and therefore cover both the brown dwarf and planetary-mass companion regimes. This was then scaled down to the expected counts in a

200 mas circle around the target.

In summary, no field in either band shows significantly more than 2% probability of finding a background star within 200 mas, and in the overwhelming majority of cases, including almost all new binary candidates and marginal detections, this figure was an order of magnitude lower. It is therefore exceedingly likely that background stars do not contribute in any way to the population of companion candidates in this survey.

4. DISCUSSION

4.1. Kernel Phase Performance

From our retrieval of existing and new binaries, we have demonstrated that kernel phase interferometry performs well in medium and wide band filters. For shorter wavelengths the PSF quality degrades increasing the errors, however in all cases space telescope data are firmly in the regime where wavefront quality is excellent and easily sufficient for the purposes of the algorithm. This method has demonstrated the delivery of very precise astrometry for medium-separation systems. If employed over multiple epochs, this will permit correspondingly accurate dynamical mass measurements for most detected binaries.

For the very closest companions, we note that the signal-to-noise ratio is lower and accordingly kernel phase yields weaker constraints on the binary parameters, which nevertheless should still permit the determination of dynamical masses. For systems whose close separation puts them beyond the diffraction limit, errors are dominated by covariance between the separation and contrast creating model ambiguity between close, bright companions and distant, fainter companions. We have shown that when multi-wavelength observations are employed, this degeneracy can be partially lifted.

4.2. Opportunities for Dynamical Mass and Radius Measurement

Adopting distance and mass estimates from Reid et al. (2006a) and Reid et al. (2008), and our own parameter estimates, typical binary objects reported here such as 2M 2351-2537 and 2M 2028+0052 would have a binary separation of ~ 1 AU and therefore orbital periods of 3 to 4 years. A follow-up campaign with LGS AO could be used to track the orbits of these binaries and dynamically determine their mass in the near term, as has already been achieved for GJ 802B in Ireland et al. (2008).

With the already-observed epochs from Reid et al. (2006a, 2008) and Bernat et al. (2010), two more epochs should be sufficient to permit a first fit to the binary parameters of each system. Targets observed in 2006 or 2008 will have completed a substantial fraction of their orbit since they were first observed; on the other hand, over a two month period they will have rotated by 6 degrees in mean anomaly, which is substantially greater than the \sim degree uncertainties in position angle obtained with kernel phase or aperture masking. These are pessimistic figures, in that the systems are early L dwarfs and include several systems substantially closer than 2 AU, which leads to correspondingly shorter orbital periods for targets of interest.

In Table 4, we present approximate masses computed using the methods of Reid et al. (2006a). These

were calculated by taking the absolute J magnitude of the new spectral class as listed in Pecaut & Mamajek (in preparation), applying J magnitude bolometric corrections from Golimowski et al. (2004) and comparing bolometric magnitudes with the 0.5, 1 and 5 Gyr isochrones from Chabrier et al. (2000). The calculated values are subject to direct uncertainties of order $\sim 0.03M_{\odot}$: despite the significant uncertainty in photometry, bolometric magnitude is a very strong function of mass and age and purely photometric uncertainties are small. On the other hand, the models used come with significant caveats, especially because brown dwarfs cool as they age: the mass estimates, given photometry, therefore depend on the assumed age of the system. Obtaining dynamical masses is key to calibrating these models brown dwarfs in general, as discussed in Section 1. These close new binaries therefore present a significant addition to the population of targets which can be followed up on short time scales.

In addition to this, many brown dwarfs are known to exhibit periodic radio or H_{α} emission, modulated by the body's rotation period, catalogued in detail in Antonova et al. (2013). The radio emission is believed to be from electron cyclotron maser instability in the brown dwarf magnetosphere (Hallinan et al. 2008; Kuznetsov et al. 2012). Knowing this rotation period and the projected rotational velocity $v \sin i$ from spectroscopic observations, it is possible then to determine the radius of the object if its spin is assumed to be perpendicular to the orbital plane of the system. This has been used by Berger et al. (2009) to determine the radius of a radio- and H_{α} - variable component of the brown dwarf binary system 2MASS J0746425+200032. This new sample of binary systems therefore also presents the opportunity to systematically study the radii of any brown dwarfs found to have radio emission. Notably, 2M 0036+1821 has a rotation period of 3.08 ± 0.05 hr as determined in Hallinan et al. (2008), and therefore presents the clearest new opportunity for radius measurement in this dataset.

4.3. Binarity Fraction in L Dwarf Sample

We now calculate the revised L-dwarf binary fraction in the 20-parsec sample. Following Reid et al. (2008), correcting for Malmquist bias requires that for statistics in a 20-parsec sample, we should consider only systems within 19 parsecs. The unbiased estimator is then simply the binary fraction observed. For uncertainties, ordinarily Poisson statistics would be used; in this case, however, the sample is too small ($N < 100$), and so binomial statistics are required (Burgasser et al. 2003).

Where Reid et al. (2008) had 8 binaries out of 64 systems observed in the nearest 20 parsecs, giving $\epsilon_b = 12.5^{+5.3}_{-3.0}\%$, five of the previously unresolved systems in the sample now support binary detections. Of these, the spectral class of 2M 2351-2537 is reclassified to L0/L1, while the increased spectroscopic distance to 2M 0045+1634 leaves it outside of 20 parsecs. Given that 2M 2028+0052 was already known to lie beyond 20 pc, 3 of these are admissible in the 20-parsec sample. Furthermore, 2M 1936-5502 supports a high-contrast fit, indicating a potential sub-L-dwarf classification, so among the new discoveries, there are 2 firm detections: 2M 0036+1821 and 2M 2351-2537. In addition to these,

we admit a detection of a companion to 2M 0355+1133 in Bernat et al. (2010), for a total of three new binaries. This yields a new binary fraction of $\epsilon_b = 17.2^{+5.7}_{-3.7}\%$. If 2M 1936-5502 is included, the binary fraction is then $18.75^{+5.8}_{-3.7}\%$.

4.4. Formation of Brown Dwarfs

A typical brown dwarf has a mass significantly below the Jeans mass of a collapsing protostellar gas cloud (Reid & Hawley 2005), and it is therefore difficult to explain the observed abundance of field brown dwarfs based on the standard Jeans collapse theory of star formation. This leads to two widely-discussed hypotheses (Basu 2012). The first, namely gravoturbulent collapse, posits that turbulent gas dynamics allows for the collapse of smaller clouds than naive analysis suggests, and therefore brown dwarfs may form in essentially the same manner as other stars. The alternative is embryo ejection, whereby gravitational interactions in a protostellar system may eject low-mass companion embryos before they accrete enough gas to achieve fusion in their cores (Bate et al. 2002). Bate & Bonnell (2005) propose that protostellar cores start out at the opacity limit for turbulent fragmentation (of order a few M_J) and proceed to accrete gas until they are ejected dynamically from the cloud. This behavior differs particularly strongly from direct turbulent collapse in the substellar regime, so that brown dwarfs are thrown out very early in the accretion process. Therefore by testing model predictions for these ultracool stars we provide one of the most stringent tests of the general validity of the Bate & Bonnell (2005) and Bate (2012) models of star formation for all stellar types.

The chief objection to direct gravitational collapse models had previously been that the collapse of such a low-mass cloud would require it to start out very dense and very cold compared to well-studied star forming regions (Reid & Hawley 2005). Recent millimeter interferometry by André et al. (2012) has caught just such a gravoturbulent collapse in the act, observing a gravitationally bound cloud of mass $\sim 0.02 - 0.03 M_\odot$. In addition this, Monin et al. (2013) report the detection of a molecular outflow from the brown dwarf binary FU Tau, which is the third young brown dwarf system found undergoing a formation process analogous to low-mass stars. With at least one example of a brown dwarf forming directly, models that do not account for this behavior must therefore be refined. Indeed, simulations by Jumper & Fisher (2012) reproduce the distribution of wide brown dwarf companions to main sequence stars as well as the population of close binaries.

On the other hand, while embryo ejection can easily account for the formation of isolated field brown dwarfs, binaries are problematic. The binarity fraction of very low mass stars can discriminate between these two models (Burgasser et al. 2007). Embryo ejection predicts a low binarity fraction in field brown dwarfs, as the gravitational interaction required would disrupt all but the most tightly bound binaries. The predicted binarity fraction is thus $< 5\%$ in the oldest models for embryo ejection (Bate et al. 2002), rising only to $8 \pm 5\%$ for systems with a primary mass in the range of 0.08 to 0.1 M_\odot in the most recent models incorporating radiative feedback (Bate 2012). The observed binarity fraction of ultracool

stars seems closer to 15% (Bouy et al. 2003; Reid et al. 2006a, 2008) which puts it into conflict with the models of Bate et al. (2002); Bate & Bonnell (2005); Bate (2012), although the authors noted that this prediction is subject to significant uncertainty.

The high binarity fraction reported in this paper is still further evidence in favour of a higher binarity rate than predicted by embryo ejection. Moreover, with the additional detections this prediction now lies several σ away from the observed value. The hybrid ejection model of Basu & Vorobyov (2012), by which still-collapsing clouds can be ejected from a protostellar disk, makes few clear predictions regarding binarity, other than that there should be few large-separation binaries. Given the results of André et al. (2012) in observing a gravitationally-collapsing brown dwarf mass object, it is not implausible to suggest that direct gravitational collapse may account for most or all field brown dwarfs.

The effect of radiative feedback in ameliorating the difficulties of modelling brown dwarf formation in Bate (2012) has been suggested by Dieterich et al. (2012) as an explanation for why the initial mass function and companion mass function changes at the hydrogen burning limit; while this idea is highly speculative, it seems likely that the identification of systems with a late main sequence primary and a brown dwarf secondary as reported in Section 3.3 will be of interest in testing this hypothesis.

5. CONCLUSIONS

We have shown that extraction and fitting to the self-calibrating kernel phase interferometric observables allows for a significant increase in the robust detection of companions and in the accuracy of best-fit parameters recovered when compared to simple inspection of images. The *Hubble Space Telescope*, or any instrument delivering good wavefront quality may benefit dramatically from such an approach.

Using the kernel phase technique on all 79 ultracool dwarfs in the combined HST samples of Reid et al. (2006a) and Reid et al. (2008), we independently recover all 10 prior detections and improve on the precision of fitted parameters such as position angle and separation by a factor of ~ 10 . Furthermore, we report 5 new binary detections missed by the original authors, 4 of which are presented here for the first time, and additionally four marginal detections of close or high contrast companions. This population forms an excellent base for dynamical studies to establish masses; a prospect particularly favored by the improved precision in parameter estimation. As well as these confident new detections, kernel phase identifies up to four more marginally-resolved close or faint companions, which may be of planetary mass.

The finding of a larger binary fraction for this sample helps shed light on the formation mechanisms of very low mass objects. The five additional ultracool binaries, if confirmed, lend further support to gravoturbulent collapse models for the formation of low-mass stars in the field.

We would like to thank I. Neill Reid, Olivier Guyon, Paul Stewart, Barnaby Norris, Anthony Cheetham, and James Allison for their interest, helpful feedback and consistent encouragement, as well as Sanjib Sharma for his

assistance. We would also like to thank the anonymous reviewer, for drawing attention to several items of recent work and whose comments helped us significantly improve this paper. Support for Program number HST-AR-12849.01-A was provided by NASA through a grant from the Space Telescope Science Institute, which is operated by the Association of Universities for Research in Astronomy, Incorporated, under NASA contract NAS5-26555. This research has made use of NASA's Astrophysics Data System.

REFERENCES

- Allen, P. R., Koerner, D. W., McElwain, M. W., Cruz, K. L., & Reid, I. N. 2007, *AJ*, 133, 971
- André, P., Ward-Thompson, D., & Greaves, J. 2012, *Science*, 337, 69
- Andrei, A. H., Smart, R. L., Penna, J. L., et al. 2011, *AJ*, 141, 54
- Antonova, A., Hallinan, G., Doyle, J. G., et al. 2013, *A&A*, 549, A131
- Aylott, B., Veitch, J., & Vecchio, A. 2009, *Classical and Quantum Gravity*, 26, 114011
- Baldwin, J. E., Haniff, C. A., Mackay, C. D., & Warner, P. J. 1986, *Nature*, 320, 595
- Basu, S. 2012, *Science*, 337, 43
- Basu, S. & Vorobyov, E. I. 2012, *ApJ*, 750, 30
- Bate, M. R. 2012, *MNRAS*, 419, 3115
- Bate, M. R. & Bonnell, I. A. 2005, *MNRAS*, 356, 1201
- Bate, M. R., Bonnell, I. A., & Bromm, V. 2002, *Monthly Notices of the Royal Astronomical Society*, 332, L65
- Berger, E., Rutledge, R. E., Phan-Bao, N., et al. 2009, *ApJ*, 695, 310
- Bernat, D., Bouchez, A. H., Ireland, M., et al. 2010, *ApJ*, 715, 724
- Bouy, H., Brandner, W., Martín, E. L., et al. 2003, *The Astronomical Journal*, 126, 1526
- Burgasser, A. J., Kirkpatrick, J. D., Reid, I. N., et al. 2003, *ApJ*, 586, 512
- Burgasser, A. J., Reid, I. N., Siegler, N., et al. 2007, *Protostars and Planets V*, 427
- Chabrier, G., Baraffe, I., Allard, F., & Hauschildt, P. 2000, *ApJ*, 542, 464
- Dahn, C. C., Harris, H. C., Vrba, F. J., et al. 2002, *AJ*, 124, 1170
- Deleuil, M., Deeg, H. J., Alonso, R., et al. 2008, *A&A*, 491, 889
- Dieterich, S. B., Henry, T. J., Golimowski, D. A., Krist, J. E., & Tanner, A. M. 2012, *AJ*, 144, 64
- Evans, T. M., Ireland, M. J., Kraus, A. L., et al. 2012, *ApJ*, 744, 120
- Faherty, J. K., Burgasser, A. J., Walter, F. M., et al. 2012, *ApJ*, 752, 56
- Feroz, F., Gair, J. R., Hobson, M. P., & Porter, E. K. 2009, *Classical and Quantum Gravity*, 26, 215003
- Golimowski, D. A., Leggett, S. K., Marley, M. S., et al. 2004, *AJ*, 127, 3516
- Grether, D. & Lineweaver, C. H. 2006, *ApJ*, 640, 1051
- Hallinan, G., Antonova, A., Doyle, J. G., et al. 2008, *ApJ*, 684, 644
- Huélamo, N., Lacour, S., Tuthill, P., et al. 2011, *A&A*, 528, L7
- Ireland, M. J. 2013, *ArXiv e-prints*
- Ireland, M. J., Kraus, A., Martinache, F., Lloyd, J. P., & Tuthill, P. G. 2008, *ApJ*, 678, 463
- Jennison, R. C. 1958, *MNRAS*, 118, 276
- Jumper, P. & Fisher, R. 2012, in *APS Meeting Abstracts*, 15003
- Kirkpatrick, J. D., Gelino, C. R., Cushing, M. C., et al. 2012, *ApJ*, 753, 156
- Kraus, A. L. & Ireland, M. J. 2012, *ApJ*, 745, 5
- Kraus, A. L., Ireland, M. J., Martinache, F., & Hillenbrand, L. A. 2011, *ApJ*, 731, 8
- Kraus, A. L., Ireland, M. J., Martinache, F., & Lloyd, J. P. 2008, *ApJ*, 679, 762
- Krist, J. E., Golimowski, D. A., Schroeder, D. J., & Henry, T. J. 1998, *PASP*, 110, 1046
- Krist, J. E., Hook, R. N., & Stoehr, F. 2011, in *Society of Photo-Optical Instrumentation Engineers (SPIE) Conference Series*, Vol. 8127, *Society of Photo-Optical Instrumentation Engineers (SPIE) Conference Series*
- Kuznetsov, A. A., Doyle, J. G., Yu, S., et al. 2012, *ApJ*, 746, 99
- Lloyd, J. P., Martinache, F., Ireland, M. J., et al. 2006, *ApJ*, 650, L131
- Marcy, G. W. & Butler, R. P. 2000, *PASP*, 112, 137
- Martinache, F. 2010, *ApJ*, 724, 464
- Martinache, F. 2011, in *Society of Photo-Optical Instrumentation Engineers (SPIE) Conference Series*, Vol. 8151, *Society of Photo-Optical Instrumentation Engineers (SPIE) Conference Series*
- Martinache, F., Lloyd, J. P., Ireland, M. J., Yamada, R. S., & Tuthill, P. G. 2007, *ApJ*, 661, 496
- Martinache, F., Rojas-Ayala, B., Ireland, M. J., Lloyd, J. P., & Tuthill, P. G. 2009, *ApJ*, 695, 1183
- Monin, J.-L., Whelan, E., Lefloch, B., Dougados, C., & Alves de Oliveira, C. 2013, *ArXiv e-prints*
- Mukherjee, P. & Parkinson, D. 2008, *International Journal of Modern Physics A*, 23, 787
- Mukherjee, P., Parkinson, D., & Liddle, A. R. 2006, *ApJ*, 638, L51
- Pecaut, M. & Mamajek, E. in preparation, *A Modern Mean Stellar Color and Effective Temperatures (Teff) Sequence for O9V-Y0V Dwarf Stars*
- Pravdo, S. H., Shaklan, S. B., Henry, T., & Benedict, G. F. 2004, *ApJ*, 617, 1323
- Reid, I. N., Cruz, K. L., Burgasser, A. J., & Liu, M. C. 2008, *AJ*, 135, 580
- Reid, I. N. & Hawley, S. L. 2005, *New light on dark stars : red dwarfs, low-mass stars, brown dwarfs (New Light on Dark Stars Red Dwarfs, Low-Mass Stars, Brown Stars, by I.N. Reid and S.L. Hawley. Springer-Praxis books in astrophysics and astronomy. Praxis Publishing Ltd, 2005. ISBN 3-540-25124-3)*
- Reid, I. N., Lewitus, E., Allen, P. R., Cruz, K. L., & Burgasser, A. J. 2006a, *AJ*, 132, 891
- Reid, I. N., Lewitus, E., Burgasser, A. J., & Cruz, K. L. 2006b, *ApJ*, 639, 1114
- Sharma, S., Bland-Hawthorn, J., Johnston, K. V., & Binney, J. 2011, *ApJ*, 730, 3
- Sivaramakrishnan, A., Tuthill, P. G., Ireland, M. J., et al. 2009, in *Presented at the Society of Photo-Optical Instrumentation Engineers (SPIE) Conference*, Vol. 7440, *Society of Photo-Optical Instrumentation Engineers (SPIE) Conference Series*
- Sivia, D. & Skilling, J. 2006, *Data Analysis: A Bayesian Tutorial*, Oxford Science Publications (OUP Oxford)
- Skilling, J. 2004, in *American Institute of Physics Conference Series*, Vol. 735, *American Institute of Physics Conference Series*, ed. R. Fischer, R. Preuss, & U. V. Toussaint, 395–405
- Stumpf, M. B., Brandner, W., Joergens, V., et al. 2010, *ApJ*, 724, 1
- Todorov, K., Luhman, K. L., & McLeod, K. K. 2010, *ApJ*, 714, L84
- Tuthill, P., Lloyd, J., Ireland, M., et al. 2006, in *Society of Photo-Optical Instrumentation Engineers (SPIE) Conference Series*, Vol. 6272, *Society of Photo-Optical Instrumentation Engineers (SPIE) Conference Series*
- Tuthill, P. G., Monnier, J. D., Danchi, W. C., Wishnow, E. H., & Haniff, C. A. 2000, *PASP*, 112, 555

6. IMAGE AND CORRELATION DIAGRAMS

The diagrams referred to in the above text are displayed below.

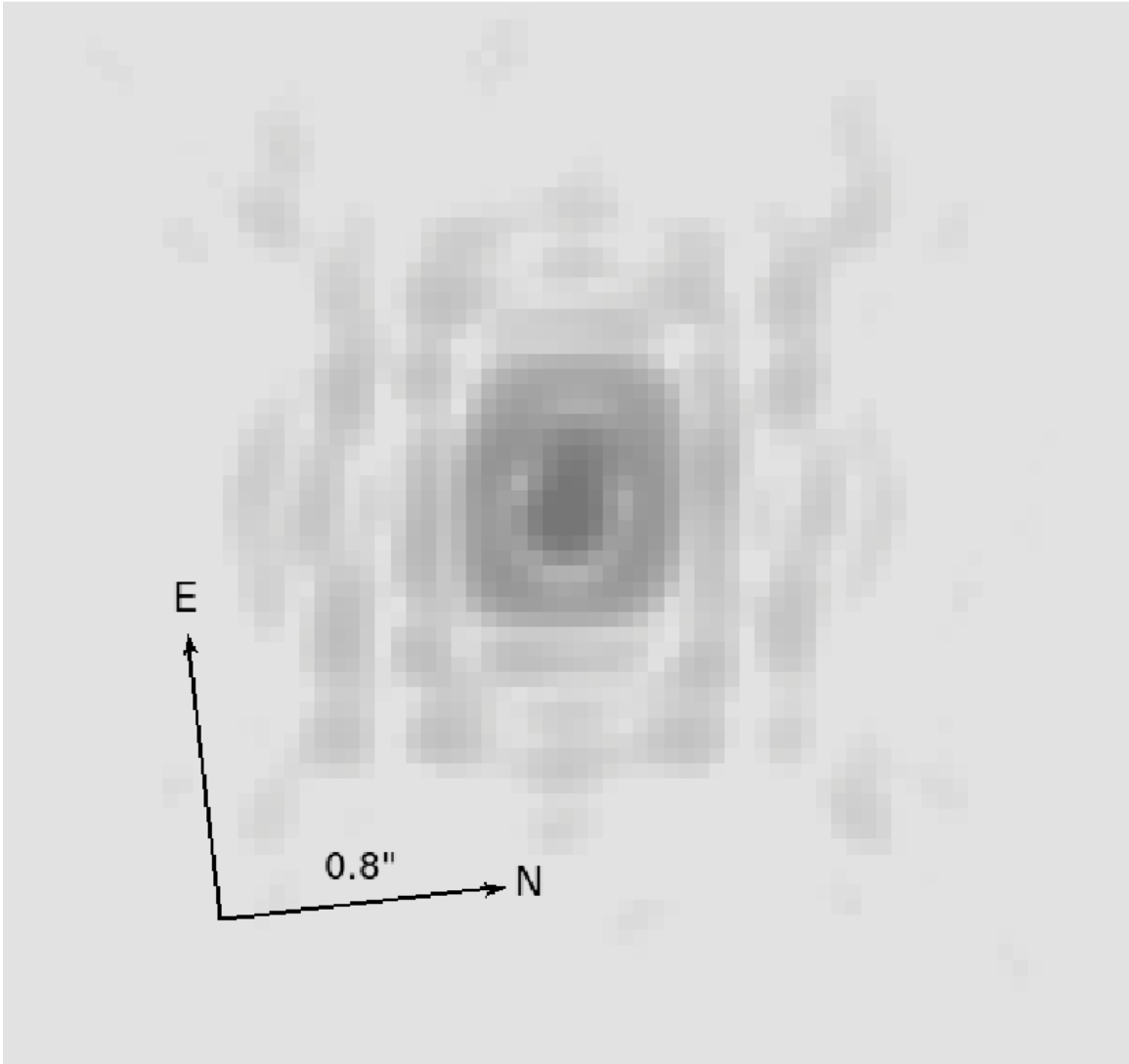


Figure 4. Log scale image of 2M 0147-4954 in F170M filter. The corresponding correlation diagrams are displayed in Figure 5. Note that while the PSFs are hard to distinguish visually, the kernel phase fit is excellent.

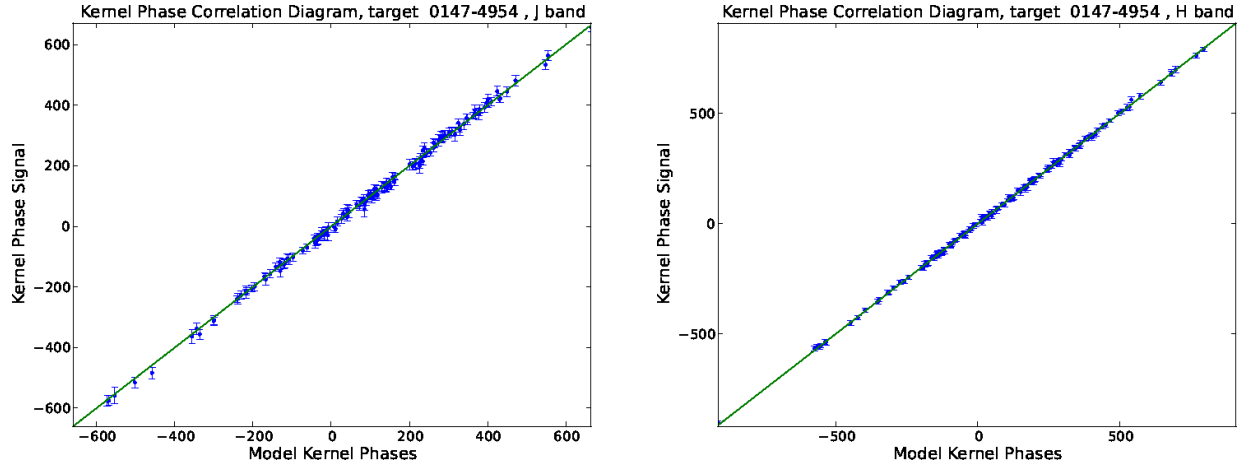


Figure 5. Correlation diagrams for the previously-detected binary 2M 0147-4954 in (left) *J* band and (right) *H* band.

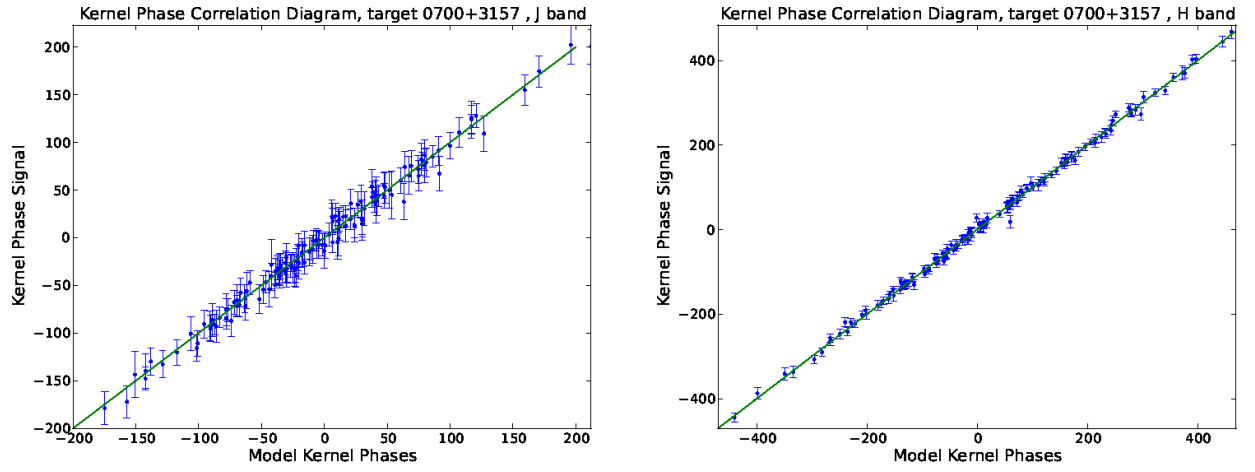


Figure 6. Correlation diagrams for the previously-detected binary 2M 0700+3157 in (left) *J* band and (right) *H* band.

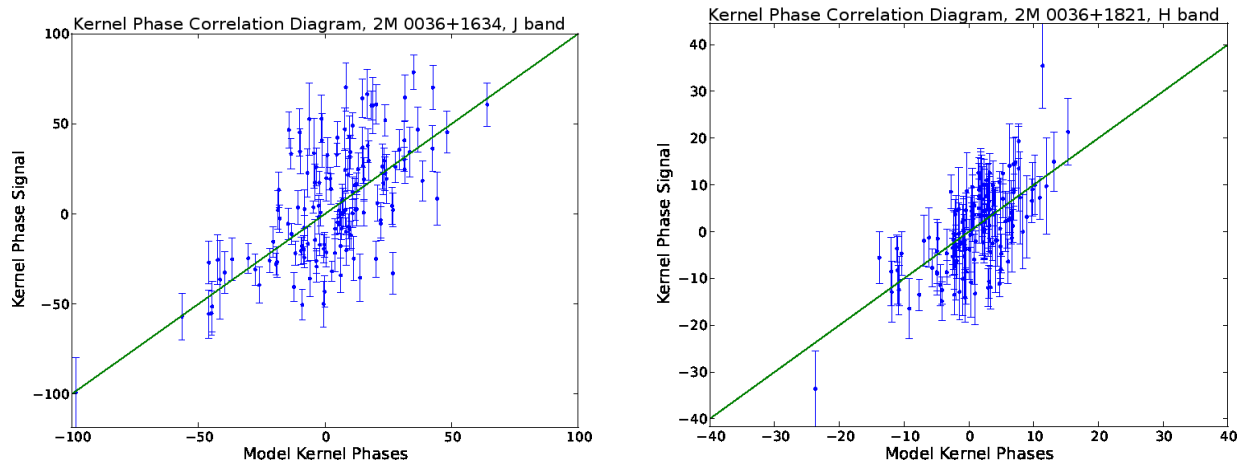


Figure 7. Kernel phase correlation diagrams for the newly-confirmed binary 2M 0036+1821 in (left) *J* band and (right) *H* band.

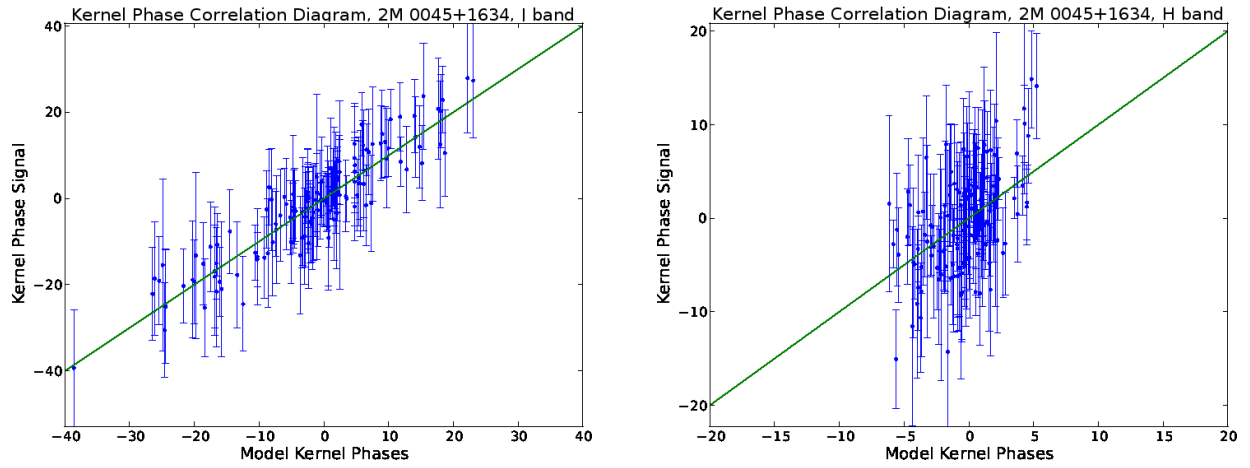


Figure 8. Kernel phase correlation diagrams for the newly-detected binary 2M 0045+1634 in (left) *J* band and (right) *H* band.

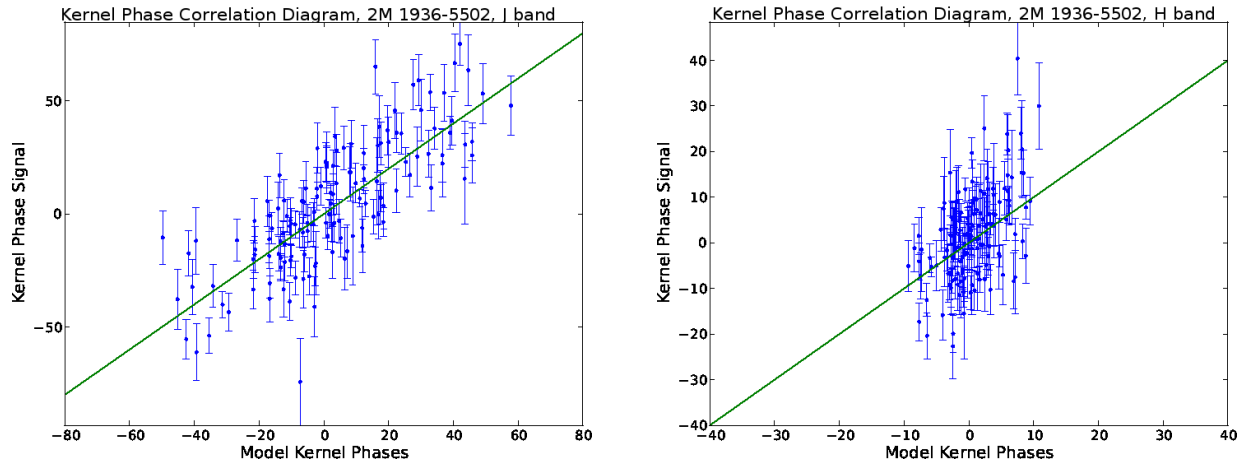


Figure 9. Kernel phase correlation diagrams for the newly-detected binary 2M 1936-5502 in (left) *J* band and (right) *H* band.

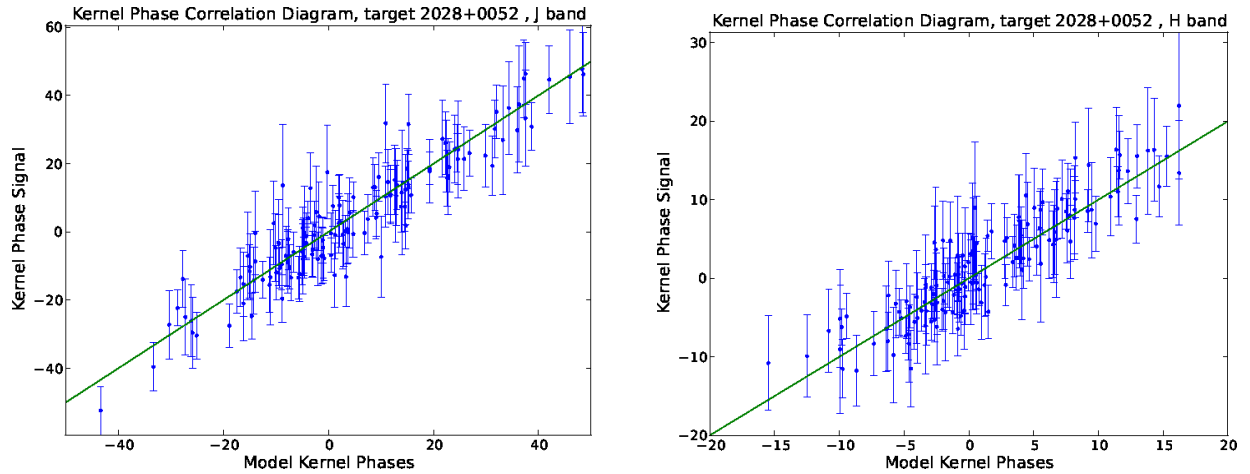


Figure 10. Correlation diagrams for the newly-detected binary 2M 2028+0052 in (left) *J* band and (right) *H* band.

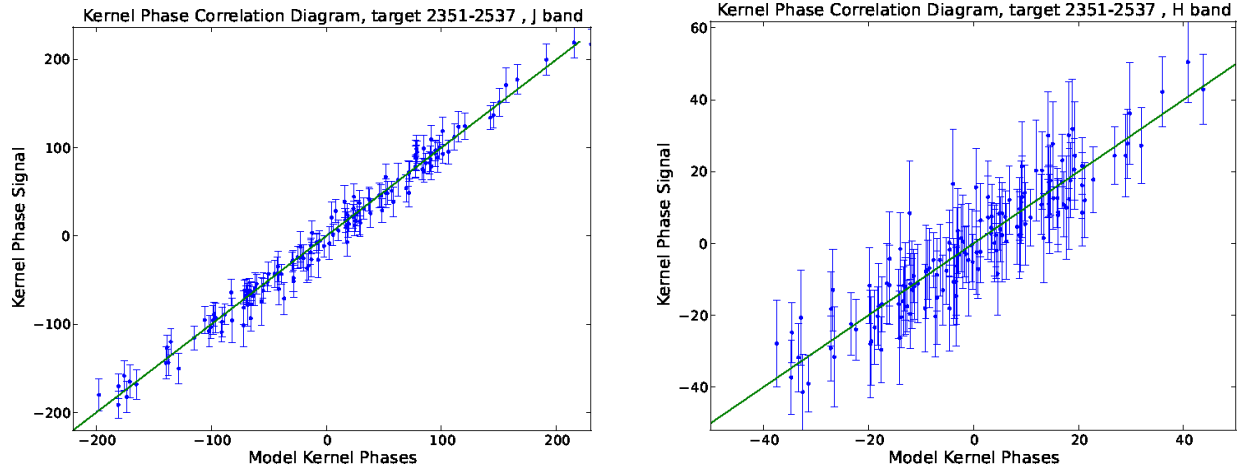


Figure 11. Correlation diagrams for the newly-detected binary 2M 2351-2537 in (left) *J* band and (right) *H* band.

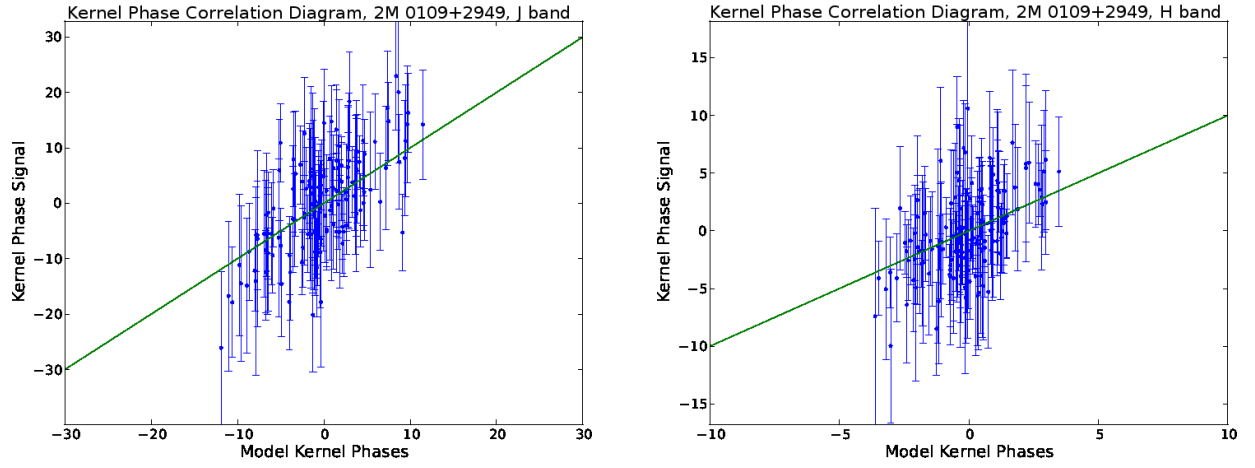


Figure 12. Kernel phase correlation diagrams for marginal detection 2M 0109+2949 in (left) *J* band and (right) *H* band.

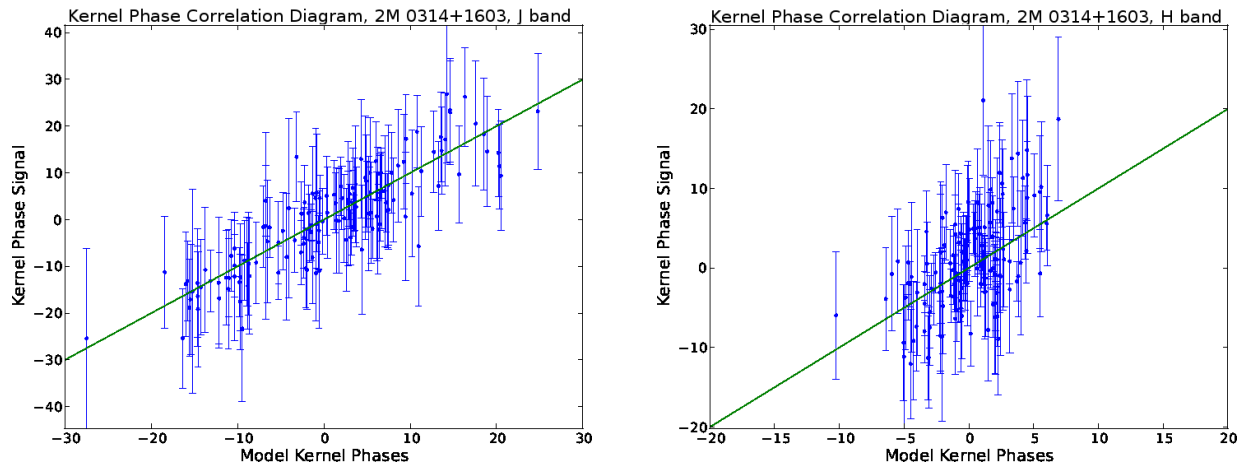


Figure 13. Kernel phase correlation diagrams for marginal detection 2M 0314+1603 in (left) *J* band and (right) *H* band.

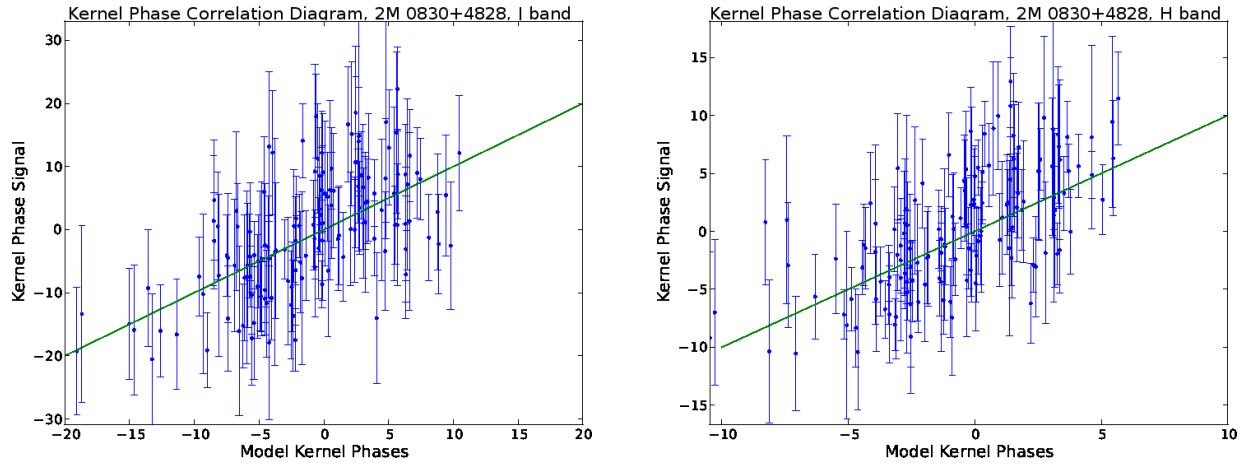


Figure 14. Kernel phase correlation diagrams for marginal detection 2M 0830+4828 in (left) *J* band and (right) *H* band.

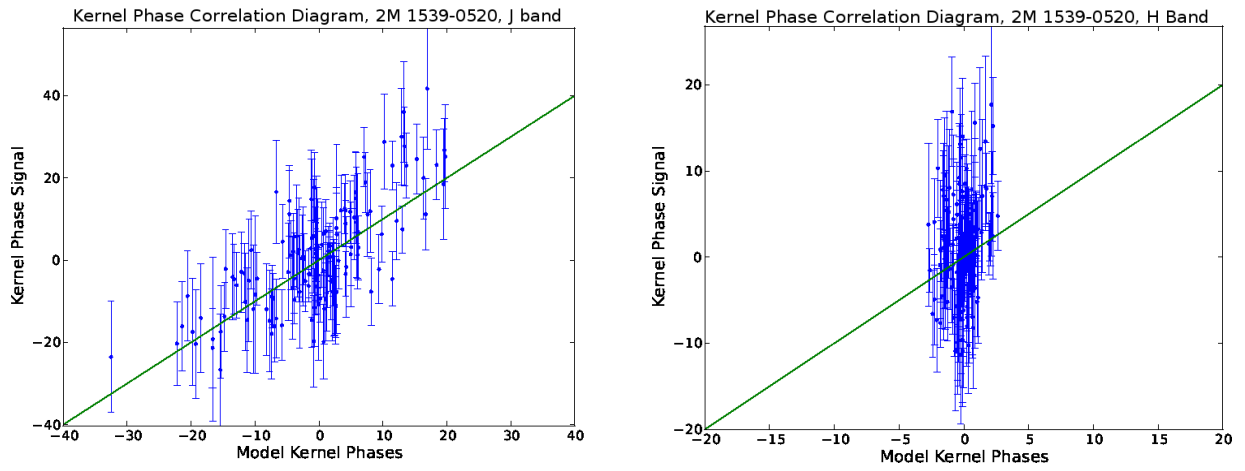
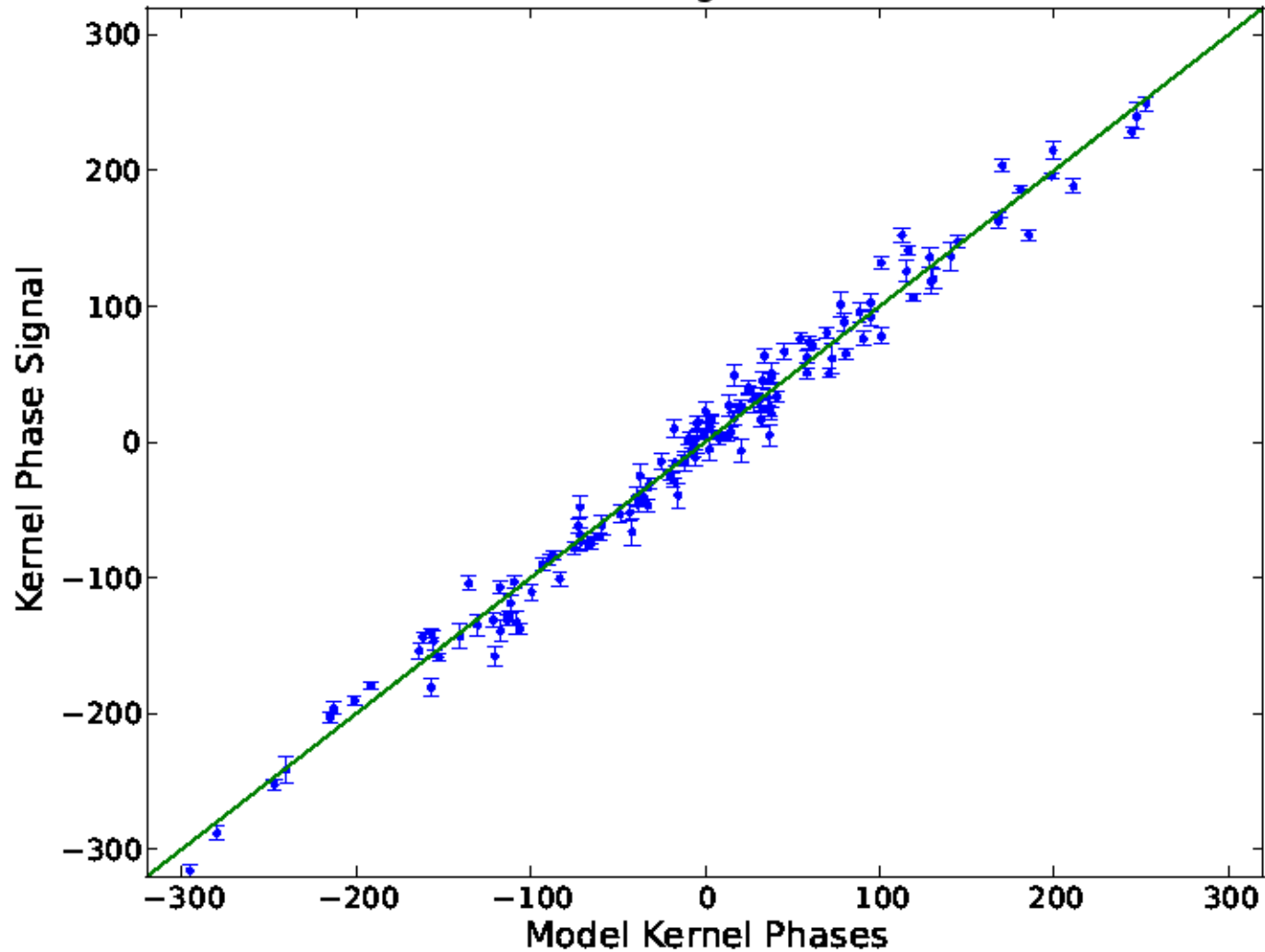


Figure 15. Kernel phase correlation diagrams for marginal detection 2M 1539-0520 in (left) *J* band and (right) *H* band.

Kernel Phase Correlation Diagram, 2M 1707-0558, H band



Kernel Phase Correlation Diagram, 2M 1707-0558, J Band

